LETTER

Operando 2D Acoustic Characterization of Lithium-Ion Battery Spatial Dynamics

Wesley Chang and Daniel Steingart*

Read Online

ACCESS | Metrics & More | Article Recommendations | Supporting Information

ABSTRACT: Spatially sensitive operando characterization techniques provide fundamental insights into dynamic and complex electrode phase behaviors of electrochemical cells during operation. However, real-time characterization of cell-level phase behavior during fast-charging has primarily been limited to synchrotron tools. We demonstrate a significant advance in the use of acoustic characterization for batteries by enabling spatially resolved operando scanning to detect local variations in phase behavior for the entire cell area during charging at all practical rates. Amplitude attenuation during fast-charge is shown to arise from localized lithium metal plating near the welded tab locations. Differential amplitude analysis takes advantage of the electrochemical-mechanical coupling of graphite staging dynamics to visualize the varying extent of graphite lithiation at different locations on the pouch cell. These time-domain modalities are coupled with frequency-domain images from Fourier transforms. Analyzing anode-free lithium metal pouch cells demonstrates that rapid and spatially heterogeneous attenuation in suboptimal electrolytes is because of electrolyte consumption initiating from electrode edges after deposition of an initial porous layer.
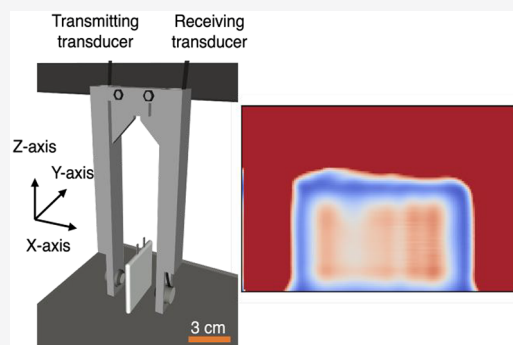
Operando 2D characterization techniques provide fundamental mechanical and chemical insights into spatial dynamics of electrochemical cells. The closed-form geometry of commercial lithium-ion cells and the fast and complex degradation mechanisms during fast charge rates introduce challenges in developing effective real-time spatially resolved characterization methods. Techniques that complement the recent advances in synchrotron X-ray imaging tools would be useful in providing a more complete mechanistic understanding of spatial and temporal dynamics in research and commercial grade electrochemical energy cells.[1−4] Specifically, nondestructive benchtop techniques that can probe internal mechanics and phase behavior of closed-form cells during cycling would bring the insights generated by synchrotron tools to most research laboratories.

We demonstrate herein a significant advance in the use of acoustics for nonionizing and noninvasive operando battery characterization. First, we develop 2D scanning modalities in both time and frequency domain that can detect localized events within the cell, pinpointing exactly where and when macroscopic heterogeneities such as lithium metal plating occur. We show the technique can detect these heterogeneities in operando, for any size and any fast-charge rate. Most importantly, we develop a differential amplitude imaging mode that resolves spatial dynamics of phase behavior, which we show arises from the coupling between cell mechanics and

electrochemistry of electrode phase transitions, a spatially resolved analog to dQ/dV.

Previous work utilizing acoustic waves of ultrasonic frequencies to probe lithium-ion cells were focused on 1D acoustic scans through one location on the cell.[5,6] In 2015, Hsieh and Steingart et al. introduced the operando electrochemical-acoustic time-of-flight technique to probe changes in cell modulus and density as a function of the acoustic wave time-of-flight.[6] This has been shown to characterize many battery chemistries and geometries, including cylindrical and pouch cells, silicon-graphite composites,[7] and degradation mechanisms, such as lithium plating[8] and cell gassing.[9−11] A 1D acoustic model along with some derivations of the wave equation demonstrated the link between acoustic time-of-flight and cell stiffness and density and showed that this can extend to any number of electrode layering due to mechanical property averaging in composite layers.[12] Some further work by Robinson et al., Deng et al., and Bauermann et al. imaged cell wetting during formation or post-mortem defects using
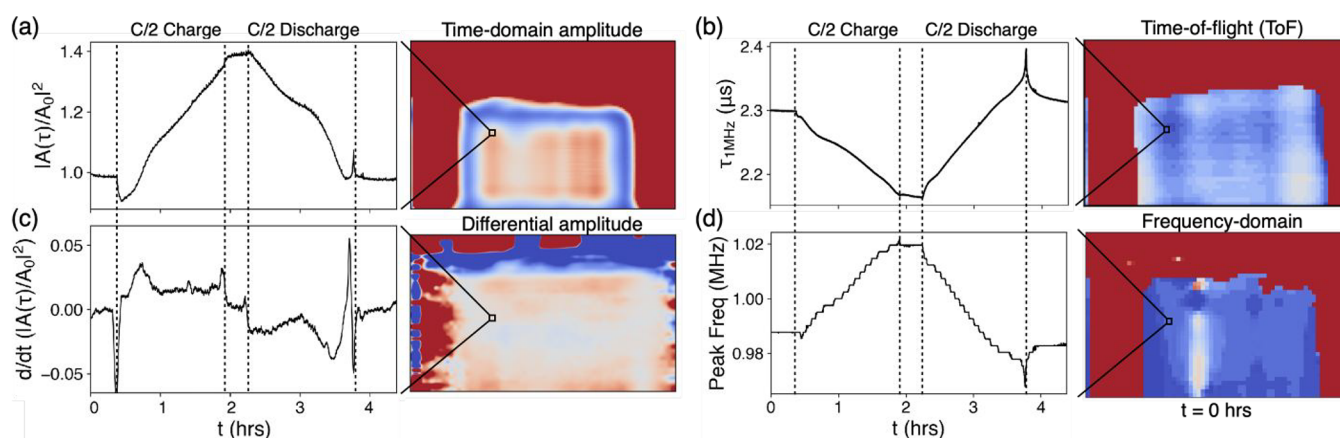
Figure 1. Acoustic scanning modalities. (a) Time-domain amplitude scanning takes the total wave amplitude intensities, with the time evolution of one point depicted through a C/2 rate charge/discharge cycle. The normalized amplitudes can be used to decouple cell packaging from cycling-induced spatial variations. (b) Time-of-flight (ToF) scanning takes the wave transmit time through the cell, which relates sound speed with cell thickness and modulus change. (c) Differential amplitude phase scanning takes advantage of the electrochemical-mechanical coupling of electrode phase transitions to image cell-level variations in phase behavior. (d) Frequency-domain scanning takes the fast Fourier transform of the wave and images the peak frequency. Example waveforms are shown in Figure S1.

ultrasound.[13−15] These prior studies were done either during cell formation before cycling or post-mortem, and a link to underlying physical behavior (e.g., graphite phase transitions) had not been established.

Figure 1 depicts the various acoustic modes developed, showing an example image at $t = 0$ before cycling, and the change during a C/2 charge/discharge cycle at one location on the cell. Time-domain amplitude analysis takes the total amplitude intensity calculated from each individual waveform (Figure 1a). In the images and corresponding movies (Movies S1−S7), the color scheme indicates increasing attenuation from warmer (red) to cooler (blue) tones, with either raw amplitude intensities or amplitude intensities normalized to the first frame. Differential amplitude takes the derivative of the total amplitude with respect to the time difference between frames, and is discussed in a later section (Figure 1b). Frequency-domain analysis maps frequency peak shifts from Fourier transforms (Figure 1d). Time-of-flight (ToF) analysis maps the wave transmit time, which relates sound speed to thickness and modulus changes, and can be used to quantify cell expansion or stiffness change (Figure 1c).[12] Total amplitude and ToF shift calculations are also explained in prior work using 1D transmission.[8,16]

As a first example, Figure 2 demonstrates 400 mAh LiCoO$_2$/graphite pouch cells (Li-Fun) cycled at C/5 (Figure 2) (C/2 in Figure S2). Acoustic transmission scans are taken at 0.5 mm intervals across a region approximately 3×2 cm in area. The raw amplitude intensities depict the change with state-of-charge and the effects of cell packaging (Movie S1, top). The first frame captured while the cell is at open-circuit-voltage (OCV) indicates that the presence of the two welded tabs through the center of the cell and the edges outside of the cell stack both cause local attenuation. Each of the waveform amplitudes is normalized to its corresponding initial amplitude to decouple cell packaging variations from cycling-induced variations. Figure 2 depicts the normalized amplitude results, showing the increase in amplitude upon charge and decrease in amplitude upon discharge, without distinguishable spatial variations (Movie S1, bottom). Every fourth frame is shown for the sake of brevity, and the reader is encouraged to view corresponding movies for the full operando results. A typical
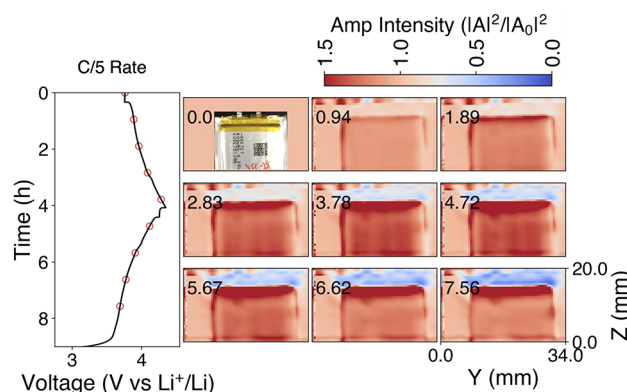
Figure 2. Operando amplitude scanning. C/5 constant current cycle for 400 mAh LiCoO$_2$/graphite pouch cell (Li-Fun). Amplitude intensities are normalized to the intensities in the first scan to decouple changes due to cycling from changes due to cell packaging. At these slow cycling rates there are minimal cycling-induced spatial variations. Similar frames for C/2 cycling are found in Figure S2. Every fourth frame is depicted, with timestamps in hours shown in the upper left corner of each frame.

lithium-ion cell stack expands in thickness upon charge, partly due to the lithiation of graphite electrodes causing volume expansion of ∼10% along with a 3-fold increase in modulus.[17] Therefore, the transmitted wave propagates through a longer pathway but results in an overall increase in the total amplitude intensity by ∼150% because of a stiffer cell stack.[16]

To demonstrate sufficient temporal resolution for scanning during fast-charging, acoustic scanning was conducted for cells cycled at 2C charge rates (constant current constant voltage protocol) to voltages of 4.2, 4.35, and 4.5 V at 25 °C (with these cells rated for 4.35 V operation). Every tenth frame for the first ∼6 h is shown in Figure 3a−c. The reader is encouraged to view the corresponding movie (Movie S2). The area on the top and sides of the cell as observed in Figure 2 are cutoff here to optimize for speed. In Figure 3a, a 2C CCCV charge rate to 4.2 V does not result in any distinguishable spatial variations. The amplitude intensities are uniform throughout the cell after five cycles, with some slight
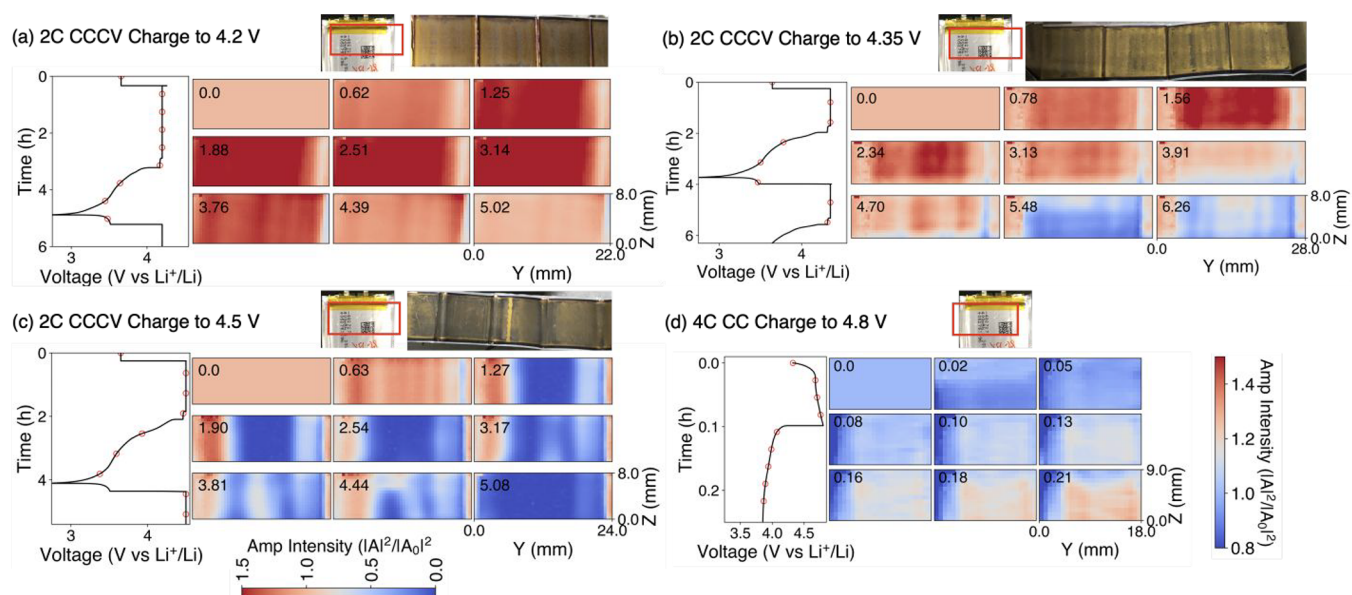
Figure 3. Operando amplitude scanning up to 4C charge rates. (a) Fast-charging (CCCV protocol) at 2C rates to 4.2, (b) 4.35, and (c) 4.5 V. Discharge rates are C/2 to 2.7 V. For brevity, every tenth frame is shown for the 2C rates. The data is best viewed in movie format in Movies S2−S4. Higher voltage cutoffs result in faster rates of attenuation and localized lithium plating at the welded tab locations in the middle of the cell. The observation of lithium plating at the tab locations is correlated with localized amplitude attenuation, which is clear for the 4.5 V cutoff test (c). These areas remain attenuated after discharge. The scanned cell region is outlined in the corresponding photos. The image intensities correspond to normalized amplitude intensities to decouple cell pack variations from cycling-induced spatial variations (note that panel d is scaled differently than panels a−c to distinguish more minor changes in intensity). (d) Amplitude imaging of a 4C constant current fast-charge to 4.8 V, followed by a 20 min OCV, with the left side corresponding to the area outside the cell stack. Attenuation is observed during the charge step and distinguishable changes are observed during the following OCV step. The cell is kept at 40 °C using a heated base in order to enable[18] this rate capability without damaging the cell. Timestamps at the upper left corners of each frame are in hours.

nonuniformity during charge on the fifth cycle (Movie S2). Cell disassembly at the top-of-charge of the fifth cycle indicates minimal presence of lithium plating (see photo in Figure 3a). In contrast, the second charge step of the 2C CCCV charge to 4.35 V presents ∼20% more attenuated amplitudes than the first charge step, as shown by the last few frames between t = 4.41 and 5.36 h in Figure 3b (in comparison with the last few frames of Figure 3a between t = 5.62 and 6.38 h). In particular, the two center regions of the cell corresponding to the locations of the tabs are ∼20% more attenuated at t = 5.04 h. This becomes even more pronounced at the end of the third charge step (>80% attenuation, Movie S3), after which cell disassembly shows substantial lithium plating localized at the same regions (see photo in Figure 3b). The most drastic rate of attenuation appears to occur during the OCV rest after the second charge step, which is indicative of plated lithium reacting with electrolyte causing cell gassing.

After cell disassembly, each of the electrodes in the cell stack exhibit lateral variations in lithium plating, which suggests differences in local stack pressure due to the effect of tab placement (see the corresponding photos in Figure 3). Prior work has shown that variations in stress due to mechanical defects, such as separator pore closure and electrode edge effects, and other thermoelectrochemical couplings leading to variations in current distribution, will affect the location and degree of lithium plating.[19−21] A 2C CCCV charge rate to 4.5 V, which is above the nominal voltage cutoff of 4.35 V for these cells, results in ∼100% amplitude attenuation on the first charge throughout the entire cell area (t = 0.95 h in Figure 3c). On the subsequent discharge step, the amplitude intensities increase by ∼50% except for the tab regions, which remain

completely attenuated (t = 3.49−4.13 h). This is indicative of irreversible lithium plating which remains on the electrode in these regions after a full discharge. Cell disassembly at the top-of-charge at 4.5 V shows lithium plating on the entire electrode region. Cell disassembly of a duplicate test after the discharge step shows localized plating along the two tab regions, which confirms the detection of irreversible plating with operando acoustic imaging (Figure S3).

On further cycling to the 4.5 V cutoff, the entire cell area becomes permanently attenuated regardless of state-of-charge (Movie S4). The decoupling of cell gassing and lithium plating acoustic signatures has been previously studied in 1D transmission.[8,10] Bommier et al. demonstrated a relationship between the acoustic time-of-flight, which is directly related to sound speed, and the degree of lithium plating. At low temperature and fast charge rates where lithium plating dominates, the acoustic time-of-flight reverses direction because of slower wave speeds through plated lithium. Chang et al. showed that cell gassing at elevated temperatures results in complete loss of signal due to the presence of solid/gas interfaces. In the case of Movie S4, permanent attenuation after five cycles even after the discharge step is indicative of significant cell gassing, as expected due to the high voltage cutoff.

Lastly, a cell cycled at 4C constant current charge rates was imaged to demonstrate the fast temporal resolution. While these cells are limited to 1C charge rates at 25 °C, an elevated temperature of 40 °C enables higher rate capability to 4C charge by increasing cell diffusivity.[18,22] Figure 3d depicts the 4C charge to 4.8 V and the subsequent OCV step. The 4C charge step results in immediate amplitude attenuation at t =
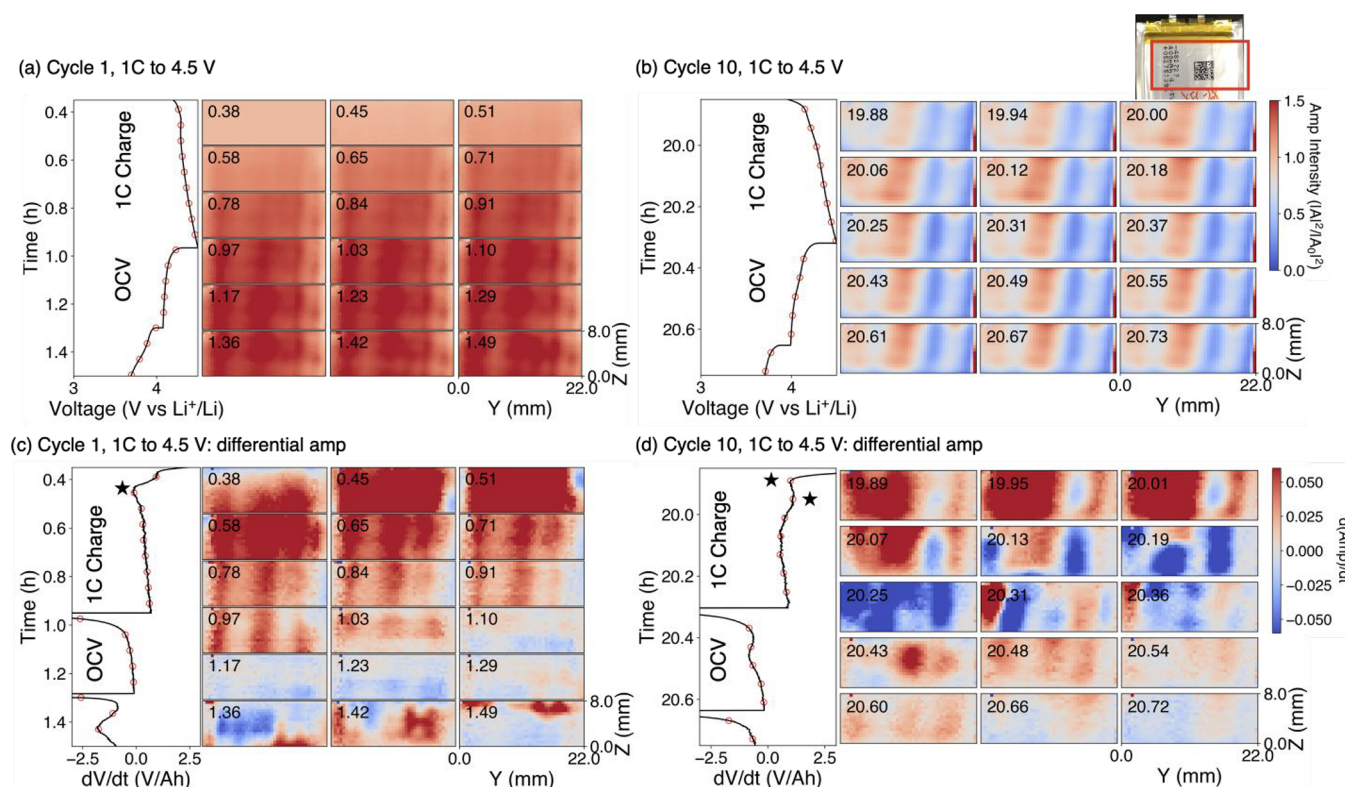
Figure 4. Differential amplitude for spatially resolved phase analysis. (a) First cycle and **(b)** 10th cycle of 400 mAh LCO/graphite pouch cell (Li-Fun) at 1C constant current charge to 4.5 V, with 20 min OCV steps and C/2 discharge. Color scheme corresponds to normalized amplitude intensities referenced to the first frame at OCV. **(c)** First cycle differential amplitude: the differential voltage peak (marked by *) on charge correlates with the differential amplitude peak between t = 0.45−0.55 h (red intensities correlate to positive differentials, blue intensities to negative differentials). The small peak upon discharge at t = 1.36 h also correlates with a shift in the differential amplitude. **(d)** At cycle 10, more spatial variations are apparent compared to cycle 1, correlated with an additional differential peak (marked by *). The full operando movie for all 25 cycles can be viewed at Movie S6.

0.02 h, followed by an increase in amplitude intensities during the rest step starting at t = 0.10 h. Further 1D analysis of rate-dependence on amplitude is described in Figure 5, which indicates that charge rates faster than 2C results in a decline in amplitude during the charge, rather than an increase. Since the amplitude attenuation recovers during the subsequent 20 min OCV (between frames at t = 0.10−0.32 h), and lithium plating should be minimal at 40 °C even at high rates, we expect that the degree of gassing and plating within the 0.1 h of charge passed is not substantial enough to permanently attenuate the waveform. The waveform amplitude decrease is correlated with a significant increase in cell expansion at 4C charge rates, as previously measured using transmission X-ray microscopy.[12] This 4C rate test shows the developed technique can image a 6 cm^2 cell area with 0.5 mm step resolution at 20 frames in 30 min or approximately 1.5 min per frame.

Following imaging at 2C fast-charge rates, a longer-term aging study was conducted at 1C charge rates with the first 40 h shown (Figure S4). The amplitude attenuates over the 40 h of cycling, with increasing attenuation rates at the tab regions (>90%, in contrast with ~50% at the center of the cell), similar to the other fast-charging results. Figure S4 depicts every 25 frames throughout the first 40 h of cycling. The full movie demonstrates the evolution of these attenuated regions over time (Movie S5). Figure 4a depicts the charge and subsequent 20 min OCV step of the first cycle and Figure 4b depicts the charge and subsequent OCV step of the tenth cycle. On the first cycle, the total amplitude intensity increases by ~150% on

charge and subsequently decreases on the C/2 discharge, similar to the other low rate cycling trends. Over many 1C charge cycles, the amplitude at any given state-of-charge gradually attenuates. At cycle 10, the increased rate of attenuation at the tabbed regions becomes clear. Since these image intensities are normalized to the initial image, cell packaging variations have already been decoupled from cycling-induced spatial variations (the raw amplitude images for the same cycles can be viewed in Figure S5). The localized attenuation at the tabbed regions is due to increased lithium plating, as observed after cell disassembly for both the 1C and 2C rate conditions. Lithium deposition may occur preferentially on the tab edges due to stress and potential concentrations created by the tab placement which causes higher local stack pressure on the electrodes.[19] After 40 h, a majority of the cell area is attenuated, which is attributed to the increased gas generation in the cell over time with continued cycling up to 4.5 V. 1D acoustic transmission was previously demonstrated to indicate lithium plating onset due to a time-of-flight shift,[8] or significant cell gassing due to complete amplitude attenuation.[10] Herein, rapid 2D scanning provides spatially resolved capabilities even for fast-charging and demonstrates the specific regions of the cell which are the majority contribution to the observed amplitude attenuation.

Acoustic imaging is prevalent in the medical field, which often uses differential spatial analysis (i.e., strain rate imaging) to visualize wall motion of organs (i.e., heart pumping).[23] This is possible because the deformation rates and phase reflections
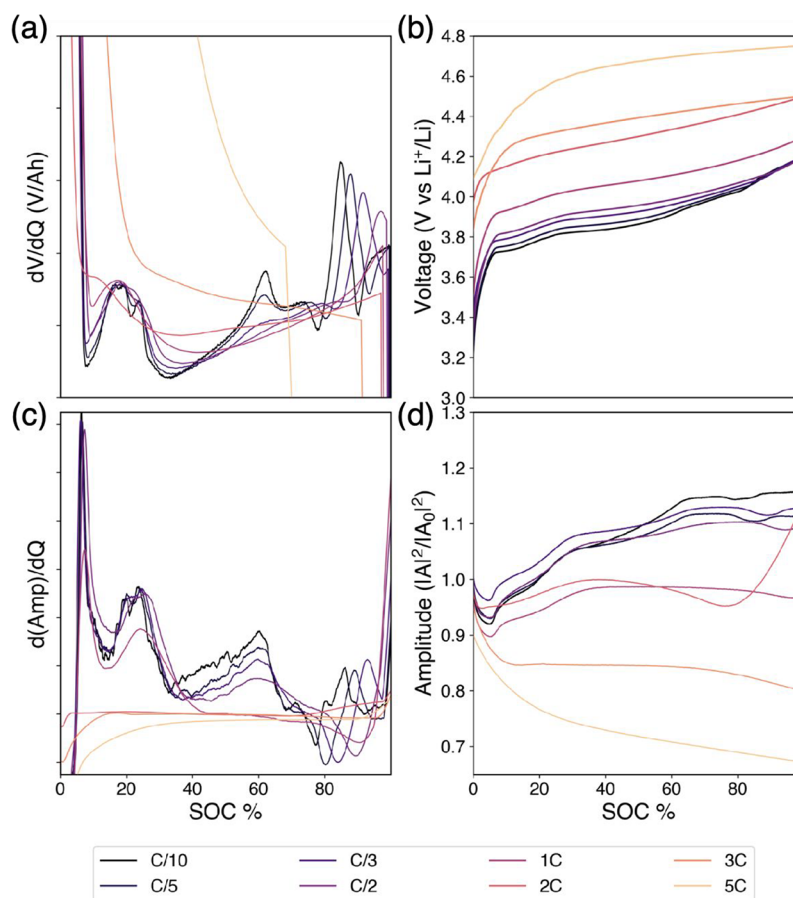
Figure 5. (a) Differential voltage (dV/dQ), (b) voltage, (c) differential amplitude ($d(Amp)/dQ$), and (d) amplitude curves during the charge step for C-rates at C/10, C/5, C/3, C/2, 1C, 2C, 3C, and 5C. The dV/dQ peaks are related to graphite phase transitions and are shown here to be almost exactly correlated with $d(Amp)/dQ$ peaks at all rates, with the fast-charge rates exhibiting broader peaks due to less distinct phase transitions.

are distinct for muscle, fat, and blood vessels. Changes in state for electrochemical cells are, however, a function of capacity or charge passed, such as the various graphite phase transitions that occur upon lithiation and delithiation. These graphite phase transitions dominate the mechanical change of a typical lithium-ion cell because of the significant 3-fold increase in graphite modulus upon full lithiation and the large structural reordering which takes place with each phase transition.[17] This is evident in differential capacity analysis (dQ/dV or dV/dQ) or differential expansion measurements, where differential capacity and expansion peaks correlate with the states-of-charge at which graphite phase transitions occur.[24,25] A typical lithium-ion full cell exhibits four primary dV/dQ peaks, which are assigned to the stage 4L to stage 3L, stage 3L to stage 2L, stage 2L to stage 2, and stage 2 to stage 1 graphite phase transitions along with some minor peaks that are related to the cathode phase change.[26] Faster charging conditions result in broader peaks because of a mixture of various phase transitions that start to occur simultaneously, with the surface of the graphite electrodes becoming lithiated faster than the region further from the surface.[25] Since voltage signatures are related to the electrochemical interface and mechanical measurements to the bulk material, some hysteresis between electrochemical and mechanical measurements are expected with higher rates because the average particle density or concentration deviates from the surface density and concentration.[27]

While dV/dQ analysis provides singular peak and phase information for the cell during cycling, differential amplitude analysis visualizes the spatial variations in phase information. Figure 4c−d depicts differential amplitude imaging frames of the cell aged at 1C to 4.5 V, for the first cycle and the tenth cycle (Movie S6). The differential voltage minimum of −0.5 V/Ah during charge at $t = 0.5$ h (Figure 4c) is shown to correlate with a maximum in the differential amplitude intensity between $t = 0.45$ and 0.55 h. The subsequent differential voltage peak upon discharge is correlated with a minor differential amplitude peak at $t = 1.36$ h. After ten cycles at the 1C charge rate, an increase in spatial variation is observed in Figure 4d. The slight hump in dV/dt at $t = 20$ h has been previously associated with a lithium plating peak,[28] and correlates with a local decrease in differential amplitude on the right side of the cell. Further, the dOCV (differential OCV) peak attributed to lithium plating at $t = 20.4$ h is correlated with local changes in differential amplitude between $t = 20.3$ and 20.45 h.[29] This is a result of phase change during the OCV step, such as diffusion of plated lithium into the graphite electrode. Movie S6 depicts the increased presence of the dOCV peak throughout 1C cycling, which is correlated with increasing spatial variations in differential amplitude during the OCV rest after charge. In the aged cell at cycle 10, the localized plating near the tab regions results in more amplitude attenuation during charge. The lower differential shift, in addition to the lower amplitude intensity, indicates
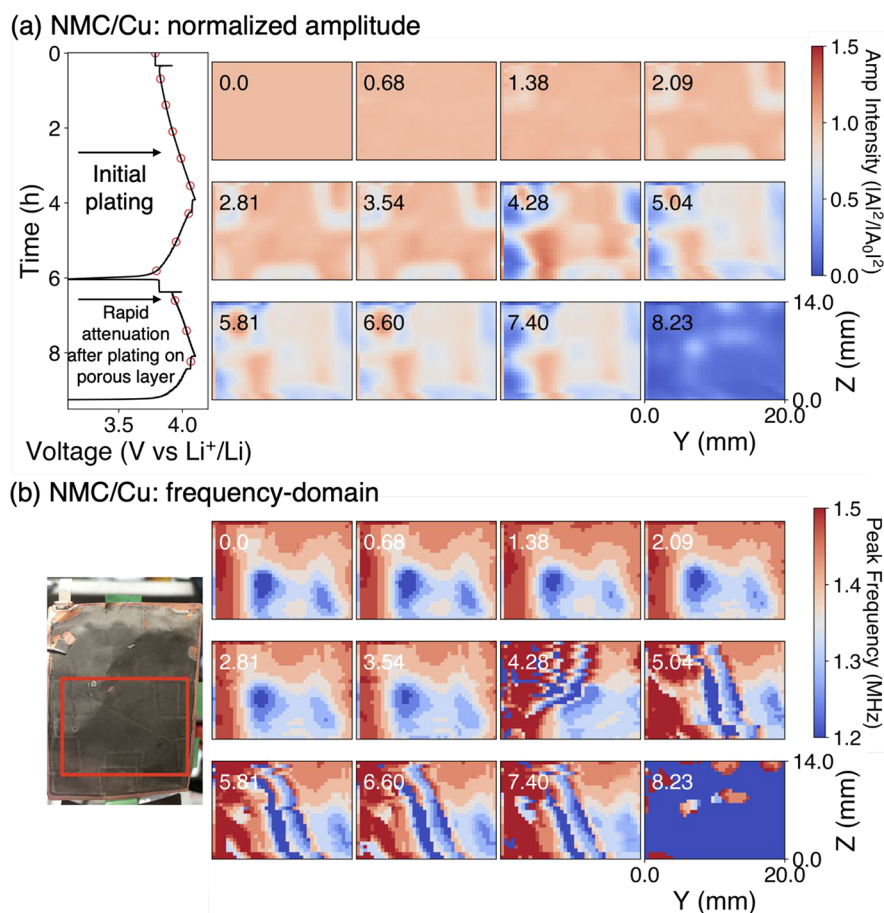
Figure 6. Operando scanning of anode-free lithium metal pouch cell. Anode-free lithium metal pouch cell with mossy and dendritic morphology (NMC532 cathode, 1 M LiPF$_6$ in EC:EMC (3:7 w/w%) + 2% VC electrolyte). (a) Time-domain amplitude scanning shows complete amplitude attenuation after deposition on initial porous layer. (b) Frequency-domain scanning of the peak frequency between 1.2 and 1.5 MHz indicates possible uneven wetting even before cycling. No external stack pressure is applied, and temperature is kept at a constant 30 °C using a heated stage. Every eighth frame is shown, with the photo indicating the scanned region.

that both localized plating, as well as lower states of lithiation contribute to these spatial variations, as differential peak shifts are related to the average bulk phase transition. Therefore, while the normalized amplitude intensity marks the overall attenuation localized to the tabbed regions over 25 cycles (Figure 4), more subtle intracycle changes due to fast-charging phase behaviors are harder to detect (Figure 4a and b) and are more finely resolved with differential amplitude imaging (Figure 4c and d).

The subsecond temporal resolution acoustic analysis technique not only captures spatial dynamics for cells cycled at all rates but also strengthens understanding of the electrochemical–mechanical coupling within cells. The peak alignment of differential voltage and differential amplitude signals is an empirical measurement of this coupling, where graphite phase transitions induce similar electrochemical and mechanical changes in the cell. To explore these coupled behaviors further, 1D acoustic transmission scans were conducted at various C-rates ranging from C/5 to 5C (Figure 5). At C/5 to 1C rates, three to four primary peaks are observed in both differential amplitude (Figure 5c) and differential voltage (Figure 5a), related to the graphite phase transitions. At rates 2C and higher, broader peaks are observed due to mixing of phase transitions and the decreased extent of lithiation resulting in decreased signal of stage 2 or stage 1 lithiated graphite. Two additional voltage signatures appear,

which may be attributed to lithium plating from prior work. First, there is a differential voltage peak (dOCV) during the OCV step after fast charge which is also observed in the differential amplitude peak. Konz et al. attributed this dOCV peak to a shift in the rate of voltage relaxation due to observable lithium plating in the prior fast-charge step.[29] The combination of lithium metal plating and lithium-ion diffusion onto and into graphite, respectively, is correlated with changes in full cell mechanics, as observed by a change in the rate of amplitude relaxation. Second, the subsequent voltage peak at the beginning of the slow discharge, previously attributed to dissolution of plated lithium,[30,31] is also observed in the acoustic amplitude. For a 1C aging test, cycle-to-cycle evolution of these two voltage signatures demonstrates significant change (Figure S6). Throughout 25 cycles, the peak shift in dOCV is correlated with the peak shift in differential amplitude. The appearance of a second peak during charge is also observed in differential amplitude. 2D differential analysis then takes these differential correlations with graphite phase transitions and maps out spatial variations at the cell-level during fast-charging. Increasing C-rates leads to differential peak broadening and a reduction in peak heights. Mohtat et al. used a multiparticle model to attribute peak broadening to greater variation in lithiation states throughout the electrode.[27] Since particles are distributed in size, the higher C-rates would preferentially lithiate the smaller particles more

than the larger particles. The differential expansion curves also experience the same peak broadening effect, though to a lesser degree, which was attributed to the fact that cell-level expansion is a bulk electrode feature rather than a surface feature. The voltage is primarily driven by the surface concentration, whereas the expansion is driven by the average concentration including the bulk, which all contribute to the total thickness change. Similarly, acoustic differentials are more sensitive to the bulk electrode than to the surface because sound waves are a function of bulk modulus and density.

Given the insights into phase evolution and other variations in spatial dynamics of lithium-ion cells, operando acoustic scanning was further conducted for anode-free lithium metal pouch cells and larger format commercial cells, both of critical importance to current battery manufacturing infrastructure.[32] Lab-scale anode-free lithium metal cells have recently been reported with electrolytes which enable decent cycle life (~200 cycles) at practically applicable energy densities (~700 Wh/L) because of the limited amount of excess lithium on the copper current collector.[33,34] There is significant focus on scaling up anode-free lithium metal cells which benefit from high cell-level energy density without excess lithium. However, rapid failure because of electrolyte consumption and an unstable lithium metal−electrolyte interface remains. In anode-free cells without graphite electrodes, the primary phase change arises from lithium metal plating on the negative current collector (formation of new phase) and electrolyte consumption (liquid to gas phase). Operando acoustic scanning maps out the rate of electrolyte consumption during cycling along with spatial variations in interfacial roughening, which acts as an acoustic scatterer. These interphasial changes, as opposed to the bulk expansion and contraction of composite graphite electrodes in lithium-ion cells, dictate the mechanical and acoustic changes in an anode-free lithium metal cell. In the case of 1 M $LiPF_6$ EC:EMC (3:7 w/w%) + 2% VC electrolyte with known poor Coulombic efficiency (CE%) and capacity retention, acoustic amplitude attenuation occurs upon the second charge cycle (Figure 6a). Attenuation initiates at the corners of the electrode stack to a limited extent on the first plating step. Following the first cycle, these locally attenuated areas rapidly propagate inward throughout the second plating step (Movie S7). Operando imaging shows that further deposition on an initial porous layer causes rapid and complete attenuation due to electrolyte consumption resulting in loss of wetting and the dispersion effect of a roughened interface. Further frequency-domain methods indicate spatial variations in peak frequencies even before cycling, which are not apparent in the time-domain images (Figure 6b). This implies the greater sensitivity of frequency to uneven wetting distribution than time-domain amplitude analysis, and the importance of conducting both modes in analysis. The areas of low frequency (below 1.25 MHz) correspond with areas of poor wetting, in contrast with the areas of higher frequency content above 1.25 MHz. The relationship between time-domain and frequency-domain signals in lithium metal cells is an avenue for further research. To investigate frequency-domain further, we revisit the Fourier transform maps for the lithium-ion cells earlier in the paper and show that peak frequencies indicate nonlinear frequency-dependencies of various cell materials (Figure S8). Fourier transforms can also be used for accurate time-of-flight measurements (Figure S7), which are useful for estimating thickness changes; these are detailed in the Supporting Information.

Cell disassembly at end of discharge confirms the irreversible formation of a porous deposited layer (Figure S9). With the addition of a minimum amount of excess lithium (30 μm foil, Honjo Lithium), acoustic amplitude attenuation as measured in 1D transmission still occurs, though to a lesser degree due to the surplus of lithium slowing down electrolyte consumption (Figure S10). In this case, the intracycle phase changes of NMC532 can also be observed cycle to cycle because of the slower attenuation rates. After 10 cycles, post-mortem scanning electron microscopy imaging for both anode-free and minimal excess lithium cases indicates substantial delamination of lithium onto the separator, which scatters the transmitted acoustic wave, reduces the amplitude intensity and causes a frequency downshift. These additional analyses further the understanding of electrolyte and electrode degradation in lithium metal cells. The operando acoustic results demonstrate that the ex situ amplitude attenuation of poorly wetted cells, as reported by Deng et al.,[14] initiates from electrode edges and then rapidly propagates throughout the entire cell area after deposition of the initial porous layer on the first cycle.

As a final note, the custom designed raster stage can image larger format commercial-scale cells. Movie S8 depicts a scaled-up temperature-regulated raster stage for operando imaging of commercial 30 A-h Li-ion pouch cells utilizing six multiplexed transducers (Figure S11 depicts 2D scans at C/5).

We demonstrate several significant advances in acoustics for battery characterization:

1. Lab-size cells (~6 cm^2) can be scanned in 2 min or less, which provides enough fidelity for operando scanning up to ~4C charge rates (or approximately 5−8 scans per 15 min fast charge).
2. Differential amplitude analysis links acoustic signals to underlying physical behavior (e.g., electrode phase transitions) a step forward from prior correlative analysis.
3. Frequency-domain is shown to be complementary to time-domain analysis in unveiling effects of various cell behaviors.
4. Operando scanning is conducted for both lithium-ion and anode-free lithium metal cells of various sizes.

■ ASSOCIATED CONTENT

ⓢ Supporting Information

The Supporting Information is available free of charge at https://pubs.acs.org/doi/10.1021/acsenergylett.1c01324.

Full experimental procedures, including an explanation of acoustic signal analyses, additional operando scanning tests, differential analysis and additional data for the 1C aging test, information on frequency-domain scanning, 1D analysis of the lithium metal cells, and 2D scanning results for the larger format cell (PDF)

Movie S1: Acoustic scanning movie depicting raw amplitude (top) and normalized amplitude intensities (bottom) at C/2 and C/5 rates (MP4)

Movie S2: Acoustic scanning movie depicting cell cycled at 2 C charge rates (constant current constant voltage protocol) to 4.2 V at 25 °C (MP4)

Movie S3: Acoustic scanning movie depicting cell cycled at 2 C charge rates (constant current constant voltage) to 4.35 V, with >80% attenuation at the third charge step (MP4)

Movie S4: Acoustic scanning movie depicting cell cycled at 2 C charge rates (constant current constant voltage) to 4.5 V with entire cell area permanently attenuated regardless of state-of-charge (MP4)

Movie S5: Acoustic scanning movie depicting cell cycled at 1 C charge rates (constant current) to 4.5 V over 40 h (MP4)

Movie S6: Corresponding differential amplitude mode for cell cycled at 1 C charge rates (constant current) to 4.5 V (MP4)

Movie S7: Acoustic scanning movie depicted for NMC/Cu cell, showing locally attenuated areas rapidly propagating inwards throughout the second plating step (MP4)

Movie S8: Scaled-up raster stage for operando scanning of large format commercial 30 A-h Li-ion pouch cells (MP4)

■ AUTHOR INFORMATION

Corresponding Author

Daniel Steingart − *Department of Chemical Engineering, Department of Earth and Environmental Engineering, and Columbia Electrochemical Energy Center, Columbia University, New York, New York 10027, United States;* ⊙ orcid.org/0000-0002-8184-9641; Email: dan.steingart@columbia.edu

Author

Wesley Chang − *Department of Mechanical and Aerospace Engineering and Andlinger Center for Energy and the Environment, Princeton University, Princeton, New Jersey 08544, United States; Department of Chemical Engineering and Columbia Electrochemical Energy Center, Columbia University, New York, New York 10027, United States;* ⊙ orcid.org/0000-0002-9389-1265

Complete contact information is available at:
https://pubs.acs.org/10.1021/acsenergylett.1c01324

Notes

The authors declare the following competing financial interest(s): D.S. is a founder of Feasible, which employs the ultrasonic technique (patent application 20160223498) used herein. Feasible did not fund the work nor participate in its execution.

■ ACKNOWLEDGMENTS

■ REFERENCES

(1) Li, W.; Lutz, D. M.; Wang, L.; Takeuchi, K. J.; Marschilok, A. C.; Takeuchi, E. S. Peering into Batteries: Electrochemical Insight Through In Situ and Operando Methods over Multiple Length Scales. *Joule* **2021**, *5* (1), 77.

(2) Yao, K. P. C.; Okasinski, J. S.; Kalaga, K.; Shkrob, I. A.; Abraham, D. P. Quantifying Lithium Concentration Gradients in the Graphite Electrode of Li-Ion Cells Using Operando Energy Dispersive X-Ray Diffraction. *Energy Environ. Sci.* **2019**, *12* (2), 656−665.

(3) Conder, J.; Marino, C.; Novák, P.; Villevieille, C. Do Imaging Techniques Add Real Value to the Development of Better Post-Li-Ion Batteries? *J. Mater. Chem. A* **2018**, *6* (8), 3304−3327.

(4) Cao, C.; Toney, M. F.; Sham, T.-K.; Harder, R.; Shearing, P. R.; Xiao, X.; Wang, J. Emerging X-Ray Imaging Technologies for Energy Materials. *Mater. Today* **2020**, *34*, 132−147.

(5) Gold, L.; Bach, T.; Virsik, W.; Schmitt, A.; Müller, J.; Staab, T. E. M.; Sextl, G. Probing Lithium-Ion Batteries' State-of-Charge Using Ultrasonic Transmission−Concept and Laboratory Testing. *J. Power Sources* **2017**, *343*, 536−544.

(6) Hsieh, A. G.; Bhadra, S.; Hertzberg, B. J.; Gjeltema, P. J.; Goy, A.; Fleischer, J. W.; Steingart, D. A. Environmental Science Electrochemical-Acoustic Time of Flight: In Operando Correlation of Physical Dynamics with Battery Charge and Health. *Energy Environ. Sci.* **2015**, *8* (5), 1569−1577.

(7) Bommier, C.; Chang, W.; Li, J.; Biswas, S.; Davies, G.; Nanda, J.; Steingart, D. Operando Acoustic Monitoring of SEI Formation and Long-Term Cycling in NMC/SiGr Composite Pouch Cells. *J. Electrochem. Soc.* **2020**, *167* (2), 020517.

(8) Bommier, C.; Chang, W.; Lu, Y.; Yeung, J.; Davies, G.; Mohr, R.; Williams, M.; Steingart, D. In Operando Acoustic Detection of Lithium Metal Plating in Commercial LiCoO2/Graphite Pouch Cells. *Cell Reports Physical Science* **2020**, *1* (4), 100035.

(9) Knehr, K. W.; Hodson, T.; Bommier, C.; Davies, G.; Kim, A.; Steingart, D. A. Understanding Full-Cell Evolution and Non-Chemical Electrode Crosstalk of Li-Ion Batteries. *Joule* **2018**, *2* (6), 1146−1159.

(10) Chang, W.; Bommier, C.; Fair, T.; Yeung, J.; Patil, S.; Steingart, D. Understanding Adverse Effects of Temperature Shifts on Li-Ion Batteries: An Operando Acoustic Study. *J. Electrochem. Soc.* **2020**, *167* (9), 090503.

(11) Pham, M. T. M.; Darst, J. J.; Finegan, D. P.; Robinson, J. B.; Heenan, T. M. M.; Kok, M. D. R.; Iacoviello, F.; Owen, R.; Walker, W. Q.; Magdysyuk, O. V.; Connolley, T.; Darcy, E.; Hinds, G.; Brett, D. J. L.; Shearing, P. R. Correlative Acoustic Time-of-Flight Spectroscopy and X-Ray Imaging to Investigate Gas-Induced Delamination in Lithium-Ion Pouch Cells during Thermal Runaway. *J. Power Sources* **2020**, *470*, 228039.

(12) Chang, W.; Mohr, R.; Kim, A.; Raj, A.; Davies, G.; Denner, K.; Park, J. H.; Steingart, D. Measuring Effective Stiffness of Li-Ion Batteries via Acoustic Signal Processing. *J. Mater. Chem. A* **2020**, *8* (32), 16624−16635.

(13) Bauermann, L. P.; Mesquita, L. V.; Bischoff, C.; Drews, M.; Fitz, O.; Heuer, A.; Biro, D. Scanning Acoustic Microscopy as a Non-Destructive Imaging Tool to Localize Defects inside Battery Cells. *Journal of Power Sources Advances* **2020**, *6*, 100035.

(14) Deng, Z.; Huang, Z.; Shen, Y.; Huang, Y.; Ding, H.; Luscombe, A.; Johnson, M.; Harlow, J. E.; Gauthier, R.; Dahn, J. R. Ultrasonic Scanning to Observe Wetting and "Unwetting" in Li-Ion Pouch Cells. *Joule* **2020**, *4* (9), 2017−2029.

(15) Robinson, J. B.; Maier, M.; Alster, G.; Compton, T.; Brett, D. J. L.; Shearing, P. R. Spatially Resolved Ultrasound Diagnostics of Li-Ion Battery Electrodes. *Phys. Chem. Chem. Phys.* **2019**, *21*, 6354−6361.

(16) Davies, G.; Knehr, K. W.; Van Tassell, B.; Hodson, T.; Biswas, S.; Hsieh, A. G.; Steingart, D. A. State of Charge and State of Health Estimation Using Electrochemical Acoustic Time of Flight Analysis. *J. Electrochem. Soc.* **2017**, *164* (12), A2746−A2755.

(17) Qi, Y.; Guo, H.; Hector, L. G.; Timmons, A. Threefold Increase in the Young's Modulus of Graphite Negative Electrode during Lithium Intercalation. *J. Electrochem. Soc.* **2010**, *157* (5), A558.

(18) Chang, W.; Bommier, C.; Mohr, R.; Steingart, D. Impact of Non-Arrhenius Temperature Behavior on the Fast-Charging Capabilities of LiCoO2−Graphite Lithium-Ion Batteries. *J. Phys. Chem. C* **2021**, *125* (3), 1731−1741.

(19) Cannarella, J.; Arnold, C. B. The Effects of Defects on Localized Plating in Lithium-Ion Batteries. *J. Electrochem. Soc.* **2015**, *162* (7), A1365.

(20) Tang, M.; Albertus, P.; Newman, J. Two-Dimensional Modeling of Lithium Deposition during Cell Charging. *J. Electrochem. Soc.* **2009**, *156* (5), A390.

(21) Fear, C.; Parmananda, M.; Kabra, V.; Carter, R.; Love, C. T.; Mukherjee, P. P. Mechanistic Underpinnings of Thermal Gradient Induced Inhomogeneity in Lithium Plating. *Energy Storage Mater.* **2021**, *35*, 500−511.

(22) Yang, X.-G.; Liu, T.; Gao, Y.; Ge, S.; Leng, Y.; Wang, D.; Wang, C.-Y. Asymmetric Temperature Modulation for Extreme Fast Charging of Lithium-Ion Batteries. *Joule* **2019**, *3* (12), 3002−3019.

(23) Heimdal, A.; Støylen, A.; Torp, H.; Skjaerpe, T. Real-Time Strain Rate Imaging of the Left Ventricle by Ultrasound. *J. Am. Soc. Echocardiogr.* **1998**, *11* (11), 1013−1019.

(24) Bloom, I.; Jansen, A. N.; Abraham, D. P.; Knuth, J.; Jones, S. A.; Battaglia, V. S.; Henriksen, G. L. Differential Voltage Analyses of High-Power, Lithium-Ion Cells: 1. Technique and Application. *J. Power Sources* **2005**, *139* (1), 295−303.

(25) Schiffer, Z. J.; Cannarella, J.; Arnold, C. B. Strain Derivatives for Practical Charge Rate Characterization of Lithium Ion Electrodes. *J. Electrochem. Soc.* **2016**, *163* (3), A427.

(26) Levi, M. D.; Aurbach, D. Diffusion Coefficients of Lithium Ions during Intercalation into Graphite Derived from the Simultaneous Measurements and Modeling of Electrochemical Impedance and Potentiostatic Intermittent Titration Characteristics of Thin Graphite Electrodes. *J. Phys. Chem. B* **1997**, *101* (23), 4641−4647.

(27) Mohtat, P.; Lee, S.; Sulzer, V.; Siegel, J. B.; Stefanopoulou, A. G. Differential Expansion and Voltage Model for Li-Ion Batteries at Practical Charging Rates. *J. Electrochem. Soc.* **2020**, *167* (11), 110561.

(28) Fear, C.; Adhikary, T.; Carter, R.; Mistry, A. N.; Love, C. T.; Mukherjee, P. P. In Operando Detection of the Onset and Mapping of Lithium Plating Regimes during Fast Charging of Lithium-Ion Batteries. *ACS Appl. Mater. Interfaces* **2020**, *12* (27), 30438−30448.

(29) Konz, Z. M.; McShane, E. J.; McCloskey, B. D. Detecting the Onset of Lithium Plating and Monitoring Fast Charging Performance with Voltage Relaxation. *ACS Energy Lett.* **2020**, *5* (6), 1750−1757.

(30) Smart, M. C.; Ratnakumar, B. V.; Whitcanack, L.; Chin, K.; Rodriguez, M.; Surampudi, S. Performance Characteristics of Lithium Ion Cells at Low Temperatures. *IEEE Aerosp. Electron. Syst. Mag.* **2002**, *17* (12), 16−20.

(31) Petzl, M.; Danzer, M. A. Nondestructive Detection, Characterization, and Quantification of Lithium Plating in Commercial Lithium-Ion Batteries. *J. Power Sources* **2014**, *254*, 80−87.

(32) Liu, J.; Bao, Z.; Cui, Y.; Dufek, E. J.; Goodenough, J. B.; Khalifah, P.; Li, Q.; Liaw, B. Y.; Liu, P.; Manthiram, A.; Meng, Y. S.; Subramanian, V. R.; Toney, M. F.; Viswanathan, V. V.; Whittingham, M. S.; Xiao, J.; Xu, W.; Yang, J.; Yang, X.-Q.; Zhang, J.-G. Pathways for Practical High-Energy Long-Cycling Lithium Metal Batteries. *Nature Energy* **2019**, *4* (3), 180−186.

(33) Louli, A. J.; Eldesoky, A.; Weber, R.; Genovese, M.; Coon, M.; deGooyer, J.; Deng, Z.; White, R. T.; Lee, J.; Rodgers, T.; Petibon, R.; Hy, S.; Cheng, S. J. H.; Dahn, J. R. Diagnosing and Correcting Anode-Free Cell Failure via Electrolyte and Morphological Analysis. *Nature Energy* **2020**, *5*, 693.

(34) Yu, Z.; Wang, H.; Kong, X.; Huang, W.; Tsao, Y.; Mackanic, D. G.; Wang, K.; Wang, X.; Huang, W.; Choudhury, S.; Zheng, Y.; Amanchukwu, C. V.; Hung, S. T.; Ma, Y.; Lomeli, E. G.; Qin, J.; Cui, Y.; Bao, Z. Molecular Design for Electrolyte Solvents Enabling Energy-Dense and Long-Cycling Lithium Metal Batteries. *Nature Energy* **2020**, *5*, 526.